© 2018. Published by The Company of Biologists Ltd | Journal of Cell Science (2018) 131, jcs212647. doi:10.1242/jcs.212647

RESEARCH ARTICLE

Septin-dependent remodeling of cortical microtubule drives cell reshaping during epithelial wound healing

Asako Shindo[1,2,*], Anastasia Audrey[1], Maki Takagishi[3], Masahide Takahashi[3], John B. Wallingford[2] and Makoto Kinoshita[1,*]

ABSTRACT

Wounds in embryos heal rapidly through contraction of the wound edges. Despite well-recognized significance of the actomyosin purse string for wound closure, roles for other cytoskeletal components are largely unknown. Here, we report that the septin cytoskeleton cooperates with actomyosin and microtubules to coordinate circumferential contraction of the wound margin and concentric elongation of wound-proximal cells in *Xenopus laevis* embryos. Microtubules reoriented radially, forming bundles along lateral cell cortices in elongating wound-proximal cells. Depletion of septin 7 (Sept7) slowed wound closure by attenuating the wound edge contraction and cell elongation. ROCK/Rho-kinase inhibitor-mediated suppression of actomyosin contractility enhanced the Sept7 phenotype, whereas the Sept7 depletion did not affect the accumulation of actomyosin at the wound edge. The cortical microtubule bundles were reduced in wound-proximal cells in Sept7 knockdown (Sept7-KD) embryos, but forced bundling of microtubules mediated by the microtubule-stabilizing protein Map7 did not rescue the Sept7-KD phenotype. Nocodazole-mediated microtubule depolymerization enhanced the Sept7-KD phenotype, suggesting that Sept7 is required for microtubule reorganization during cell elongation. Our findings indicate that septins are required for the rapid wound closure by facilitating cortical microtubule reorganization and the concentric elongation of surrounding cells.

KEY WORDS: Cytoskeleton, Embryonic wound healing, Epidermis, *Xenopus laevis*

INTRODUCTION

During wound closure in embryonic tissues, the surrounding cells form an actomyosin purse string at the wound edge, as first observed in chick wing bud (Martin and Lewis, 1992; Martin, 1997). This actomyosin purse string was considered to generate the contractile force that is able to shrink the wound edge by activation of the small GTPase Rho (Brock et al., 1996). Similar mechanisms have been observed in *Drosophila melanogaster* embryos (Abreu-Blanco et al., 2011; Zulueta-Coarasa et al., 2014; Brock et al., 2012), suggesting that the actomyosin purse string is a conserved force that drives wound closure in embryonic tissues.

Embryos utilize actomyosin contractility for various morphological processes to move cells, including apical constriction for neural tube closure (Haigo et al., 2003), bottle cell formation during gastrulation (Lee, 2012) and collective cell movements of convergent extension (Zallen and Wieschaus, 2004; Nishimura et al., 2012; Shindo and Wallingford, 2014). Actomyosin contractility is a widely conserved process of morphogenesis. Notably, actomyosin at the wound edge causes cell movements within seconds (Soto et al., 2013), whereas other developmental processes occur over several hours.

The functional interaction with microtubules might be necessary for the dramatically rapid actomyosin effects during wound closure. In particular, a single-cell wound-healing study in which *Xenopus laevis* oocytes were used, indicated that the microtubules are indispensable for the trafficking and recruitment of actin to the wound edge (Bement et al., 1999; Mandato and Bement, 2003). A study in which *D. melanogaster* embryos were used also revealed that the disruption of microtubule dynamics in an end-binding protein 1 (EB1) mutant resulted in slower wound closure, with a delay of actomyosin assembly at the wound edge in multi-cellular wounds (Abreu-Blanco et al., 2012). These studies indicate that actomyosin cooperates with microtubules during embryonic wound closure. However, it remains unknown how this combinatory contribution to the rapid wound closure in vertebrate embryonic tissues is achieved.

One possibility is through septins, which comprise a group of GTP-binding proteins that cooperate with actomyosin and microtubules (Kinoshita et al., 1997; Spiliotis, 2010; Bowen et al., 2011; Sellin et al., 2012). Septins are highly conserved in eukaryotic cells of fungi, animals and a number of green algae (Sirajuddin et al., 2007; Weirich et al., 2008). The number of septin genes is extensive in different organisms; for example, *Caenorhabditis elegans* has only two septins, whereas the human genome encodes 13 septin genes. Septins show either ubiquitous or tissue-specific distribution and are classified into groups based on sequence and domain homologies. Septins were found to associate with actomyosin and microtubules in *in vitro* studies using e.g. HeLa, MDCK and PC12 cells (Surka et al., 2002; Kremer et al., 2005; Bai et al., 2013). When septins are used as scaffolding or partition proteins in a cell, actomyosin localization and contraction have been shown to be locally restricted (Joo et al., 2007; Mostowy and Cossart, 2012; Shindo and Wallingford, 2014; Wasik et al., 2017).

In our current study, we examined cell edge contraction and cell elongation – key events for rapid closure of the embryonic wound – to address the contribution of each cytoskeleton. By using the *X. laevis* neurula, a vertebrate model amenable for cellular imaging, we focused on septins as candidates to achieve the combinatory contribution of actomyosin and microtubules to the cell behaviors. In particular, we investigated the role of septin7 (Sept7) by utilizing

[1]Division of Biological Sciences, Department of Molecular Biology, Nagoya University Graduate School of Science, Nagoya 464-8602, Japan. [2]Department of Molecular Biosciences, University of Texas at Austin, Austin 78712, USA. [3]Department of Tumor Pathology, Nagoya University Graduate School of Medicine, Nagoya 466-8550, Japan.

*Authors for correspondence (shindo.asako@f.mbox.nagoya-u.ac.jp; kinoshita.makoto@c.mbox.nagoya-u.ac.jp)

A.S., 0000-0002-3314-7151; M.K., 0000-0002-7592-2400

Received 30 October 2017; Accepted 10 May 2018

Journal of Cell Science (2018) 131, jcs212647. doi:10.1242/jcs.212647

a previously developed Sept7 knockdown (Sept7-KD) *X. laevis* model generated with a morpholino antisense oligo (MO) and pharmacological inhibition (Kim et al., 2010; Shindo and Wallingford, 2014). Wound closure rates and phenotypic changes of cells were compared between Sept7-KD and control embryos over time. Live imaging and immunostaining were used to determine the functional interaction and association of Sept7 with the actomyosin purse string, and with microtubules during the wound healing process. Our findings clarify the role of Sept7 for the functional interactions of actomyosin and microtubules that, in turn, cause rapid cell behaviors during wound closure across mammalian embryos.

RESULTS

Cells elongate radially toward the center of the wound in minutes

Elongated cells were first observed in vertebrate embryonic wound closure by scanning electron microscopy (Stanisstreet et al., 1980; McCluskey and Martin, 1995; Lawson and England, 1998); however, it was not known how rapidly the cells elongate after wounding. We created wounds by aspirating a diameter of ∼100 µm (equivalent to the area of 20–30 cells) of the superficial epidermal layer in live *X. laevis* neurula, and observed the process of wound closure by using stereomicroscopy (Fig. 1A) and confocal microscopy (Fig. 1B,C). The wound closed in ∼20 min through cell elongations that were initiated within 3 min after wounding (Fig. 1B,C). The cells continued elongation until the ellipticity (i.e. the length-to-width ratio) of the cells reached ∼3.6 on average (Fig. 1D). As the cell elongates, it edges along the wound margin (wound edge length) and shortens by approximately one-third within 5–15 min after wounding (Fig. 1E). As previously reported in a study by Davidson et al. (2002) in which they examined the *X. laevis* animal pole, we observed F-actin accumulation at the wound margin (Fig. 1B, arrows).

Such rapid changes in cell shape were also observed in mouse embryos (Fig. S1). Specifically, we created a circular wound ∼100 µm in diameter, similar to the size of the wound in *X. laevis* shown in Fig. 1, in the lateral epidermis of mouse embryos at embryonic stage 9 (E9). The wounded embryos were fixed at 5 or 20 min after wounding for immunostaining using phalloidin and wheat germ agglutinin (WGA). Phalloidin stained the wound edge, suggesting the formation of an actin purse string (Fig. S1A,B), as reported previously for later-phase wound closure in E11.5 stage embryos (McCluskey and Martin, 1995). The cells exhibited an ∼1.7-fold increase of ellipticity (Fig. S1C) as the cell edges at the wound margin shortened ∼8.6 µm on average within 5–20 min (Fig. S1D). Taken together, cell shape changes occurring around the wound margin within minutes are evolutionally conserved in vertebrates as well as in invertebrate embryos, as reported previously (Abreu-Blanco et al., 2012).

Microtubules are required for cell elongation

Although the actomyosin purse string and its interaction with microtubules have been well studied in single-cell wound healing (Mandato and Bement, 2003), the role of microtubules in multicellular wound closure has not yet been fully investigated. To determine the significance of microtubules for the observed cell behaviors shown in Fig. 1, we disrupted microtubules in multiple ways, and analyzed their effects on wound edge contraction and cell elongation.

We performed pharmacological inhibition of tubulin polymerization by using nocodazole. Nocodazole treatment slowed the reduction in the wound area (Fig. S2A) and also attenuated cell elongation, as represented by the ellipticity of each

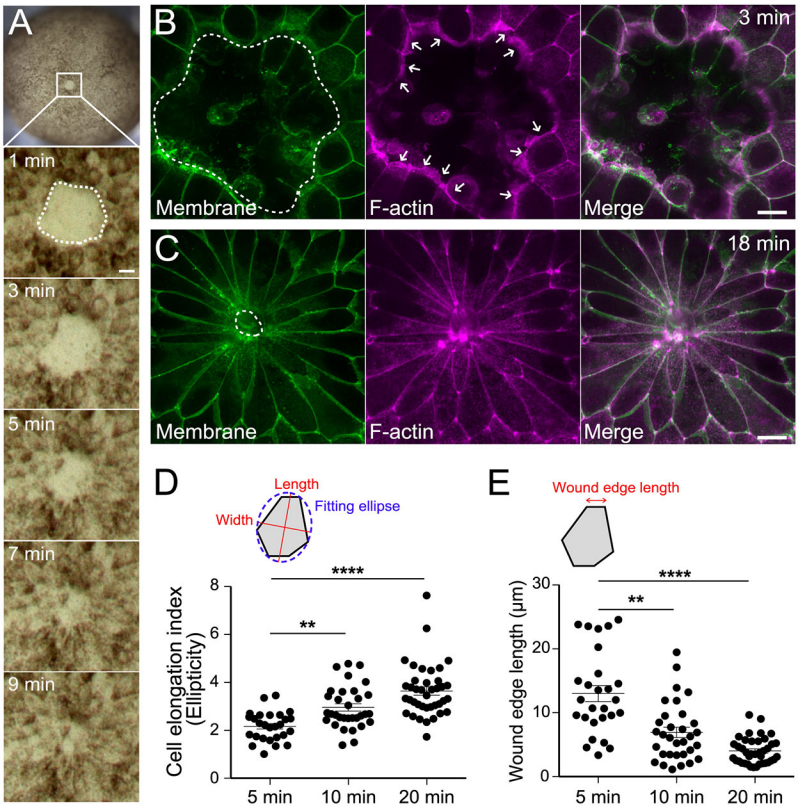

Fig. 1. Cells elongate radially toward the center of the wound. (A) Stereoscope images of the wound made in the epidermal tissue of *X. laevis* neurula; stills were taken every 2 min from time-lapse movies. Only the outer layer was peeled off. The brown sheet is the outer layer of the epidermis and the paler region shows the exposed deeper layer. The wound edge is surrounded by a dotted line. (B,C) Fluorescence images of wounded embryos injected with membrane-BFP (green) and Lifeact-RFP (F-actin, magenta). Images in B were taken at 3 min after wounding, those in C at 18 min after wounding. Dotted lines surround the wound edge, arrows indicate F-actin accumulation at the wound margin. (D) Quantification of cell elongation during live imaging. The cell elongation index was calculated according to the ellipticity (length:width ratio) of each cell. The *x*-axis indicates the time after wounding. 5 min (n=27), 10 min (n=33), 20 min (n=39) from 4 embryos. (****P<0.0001, **P=0.0037, one-way ANOVA was applied, followed by the Kruskal–Wallis test for multiple comparisons). (E) Quantification of the length of the cell edge facing the wound. The *x*-axis indicates the time after wounding. 5 min (n=27), 10 min (n=32), 20 min (n=39) from 4 embryos. (****P<0.0001, **P=0.0013, one-way ANOVA was applied, followed by the Kruskal–Wallis test for multiple comparisons). Scale bars: 20 µm.

Journal of Cell Science (2018) 131, jcs212647. doi:10.1242/jcs.212647

cell. The inhibitor of Rho-associated kinase Y27632 had similar effects (Fig. 2A–C′,D). The wound edge in each cell was longer in nocodazole-treated embryos at each time point when compared with that of control embryos (Fig. 2E). The length of the wound edge at 3 minutes after wounding was increased in nocodazole-treated embryos (Fig. 2E–G). However, although the velocity of wound edge shortening in each cell was normal (Fig. 2F,H), elongation of the lateral edge was slower in nocodazole-treated embryos (Fig. 2F,I). These data suggest that the less ellipticity was observed because the lateral edges elongated less. Notably, a mixture of nocodazole and Y27632 showed additive effects both for cell elongation and wound edge dynamics (Fig. 2D,E). Moreover, accumulation of F-actin and phosphorylated myosin light chain (pMLC), a marker of activation of actomyosin contractility, at the wound edge was still observed in embryos treated with nocodazole (Fig. S2B–D).

Microtubules reorient during wound closure

To address how the microtubules might be involved in the process of cell shape changes during wound closure, we next visualized microtubules in intact and wounded epidermis. We observed that microtubules radially reorganize and form thicker bundles at 4–5-µm depth from the apical surfaces along cell cortices after wounding in *X. laevis* neurula (Fig. 3). In intact epidermis, both live imaging and immunostaining of α-tubulin indicated the presence of few filaments in each field (Fig. 3A,A′, dotted arrowheads; Fig. S3A). In contrast, microtubules formed more bundles along cell cortices in wounded epidermis (Fig. 3B–C′, Fig. S3B). The mean intensity of α-tubulin markers along the cell cortices in live and fixed embryos reflected the existence of microtubule bundles in the wounded tissues (Fig. 3D,E). Notably, the mean intensity of α-tubulin markers along the cell membrane did not show obvious differences between the phases during wound closure (data not shown). In contrast, the formation of cortical microtubule bundles was obvious in the later phase through the formation of more bundles along cell cortices (Fig. 3C,C′, arrowheads). Together, these data suggest that the wounding triggers microtubule reorganization leading to bundle formation along cell cortices.

Sept7 is required for rapid wound closure by controlling cell shape changes at the wound margin

The actomyosin purse string and cortical microtubules, therefore, appear to coordinate in order to achieve the rapid cellular response after wounding. We next directed our attention to the septin family of proteins, comprising cytoskeletal components that are capable of interacting with both actin and microtubules, to address the mechanism underlying the coordination of these two cytoskeletal systems (Spiliotis, 2010; Bowen et al., 2011; Sellin et al., 2012). In particular, we focused on Sept7 because it constitutes a core subunit of septin heterooligomers. We investigated the function(s) of Sept7 for wound closure by utilizing our previously reported *X. laevis* Sept7 knockdown (Sept7-KD) embryo model (Kim et al., 2010; Shindo and Wallingford, 2014).

The wound area in wild-type (control) embryos temporarily reduced within 1 min after wounding and then quickly expanded the following minute (Fig. 4A, black line); this is comparable to a previously reported ‘reduction-expansion’ process (Abreu-Blanco et al., 2012). In our experiments, the wound area in control embryos then decreased to half of the original size within 4 min, and continuously reduced throughout the observation time (between 10 s and 23 min after wounding). In contrast, Sept7-KD

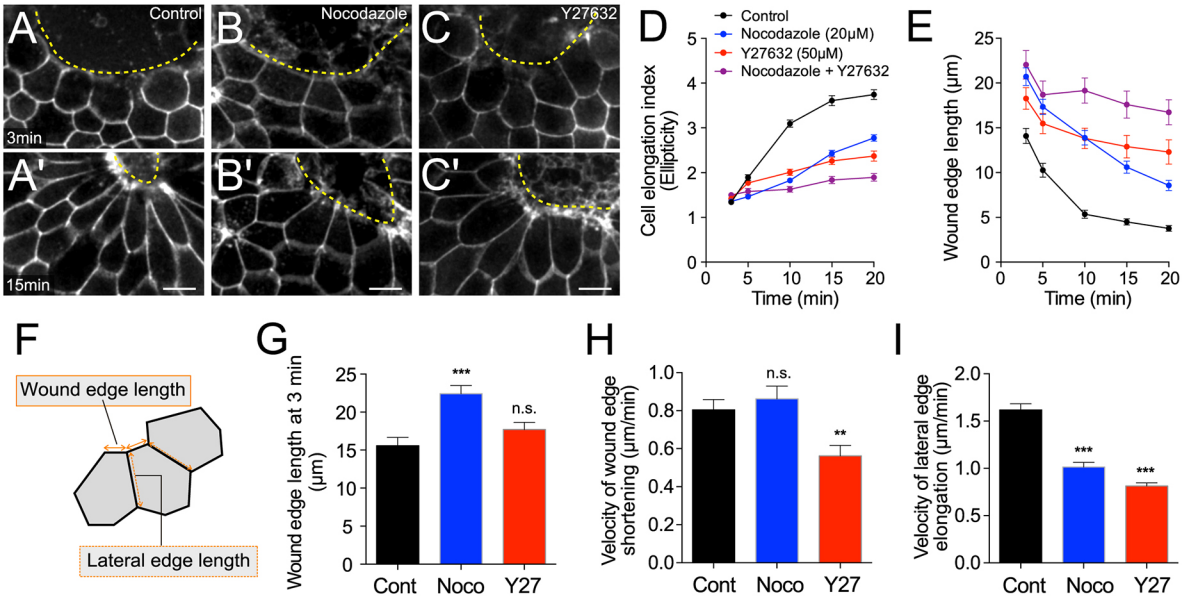

Fig. 2. Microtubules are required for cell elongation during wound closure. (A–C′) Still fluorescence images from time-lapse imaging of control (A,A′), nocodazole- (B,B′) or Y27632-treated embryos (C,C′) at 3 min (A,B,C) or 15 min (A′,B′,C′) after wounding. Embryos express membrane-BFP. Scale bars: 20 µm. Dotted lines indicate the wound edge. (D) Quantification of cell elongation by measuring the ellipticity of each cell. (P<0.0001, two-way ANOVA followed by Dunnett’s test for multiple comparisons. Control: n=68 from 3 embryos; nocodazole: n=74 from 4 embryos; Y27632: n=73 from 4 embryos; nocodazole+Y27632: n=50 from 3 embryos). (E) Quantification of wound edge shortening of each cell. Control (black), nocodazole-treated (blue), Y27632-treated (red), and mixture of nocodazole and Y27632-treated embryos (purple). (P<0.0001, two-way ANOVA followed by Dunnett’s test for multiple comparisons. Control: n=51 from 3 embryos; nocodazole: n=70 from 4 embryos; Y27632: n=78 from 4 embryos; nocodazole+Y27632: n=41 from 3 embryos). (F) Schematic of wound edge and lateral edge of each cell as measured in G–I. (G) Comparison of avarage wound edge length in each cell at 3 minutes after wounding. (***P=0.0002, Control (Cont): n=48 from 3 embryos, nocodazole (Noco): n=62 from 4 embryos, Y27632 (Y27): n=87 from 4 embryos). (H,I) Comparison of average velocity of wound edge shortening (H) or lateral edge elongation (I) at 3–10 min after wounding. (**P=0.0054, ***P<0.0001, one-way ANOVA followed by the Kruskal–Wallis test for multiple comparisons, Cont: n=45 from 3 embryos, Noco: n=72 from 4 embryos, Y27: n=79 from 4 embryos).

Journal of Cell Science (2018) 131, jcs212647. doi:10.1242/jcs.212647

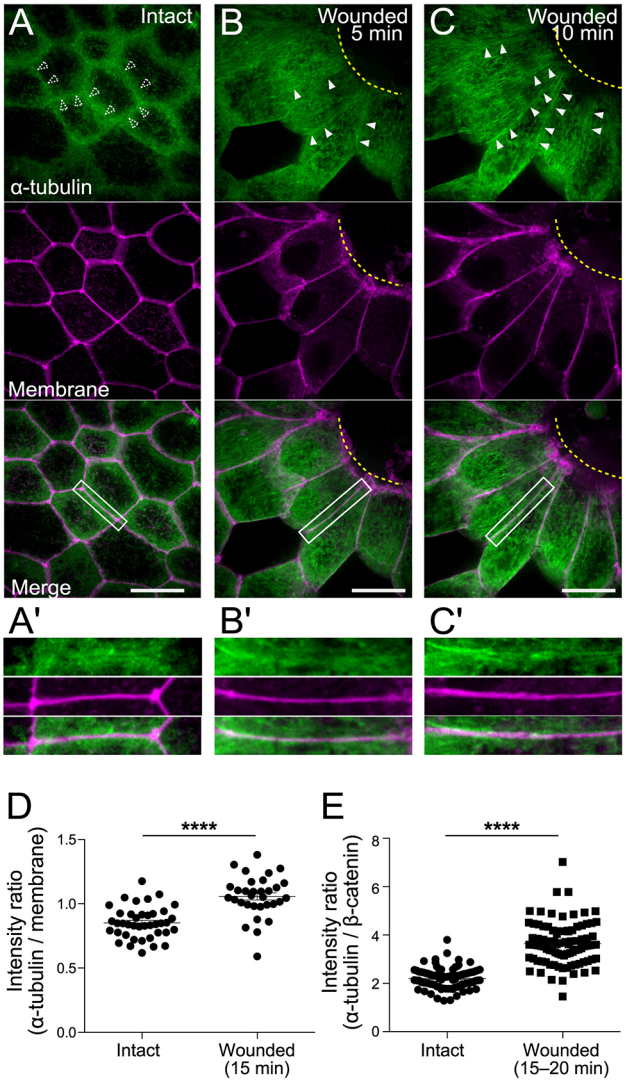

Fig. 3. Microtubules reorient during wound closure. (A–C′) Fluorescence images of maximum intensity *z*-projections of 10-µm thick intact epidermis (A), 5 min after wounding (B) and 10 min after wounding (C) in *X. laevis* neurula injected with α-tubulin-emerald GFP (green) and membrane RFP (magenta). Dotted arrowheads indicate lack of filaments. Arrowheads indicate microtubule filaments along the lateral cell cortices. A′,B′,C′ are magnified images of single cell–cell junctions (boxed areas in A,B,C, respectively). Dotted lines indicates the wound edge. (D) Microtubule filament formation along cell cortices was quantified by the ratio of α-tubulin-emerald GFP and membrane-RFP. The mean intensity of each marker was measured along the cell–cell junctions with 1-µm width using ImageJ (****P<0.0001, Student's *t*-test, Intact: n=40 from 3 embryos, Wounded n=32 from 2 embryos). (E) Same analysis as shown in D but of fixed embryos stained with α-tubulin and β-catenin antibodies shown in Fig. S3. (****P<0.0001, Mann–Whitney *U*-test, n=90 from 3 embryos, Wounded n=90 from 2 embryos). Random sampling was performed by using software from the free software environment R (https://www.r-project.org/); original number was 241 (intact) and 98 (wounded). Scale bars: 20 µm.

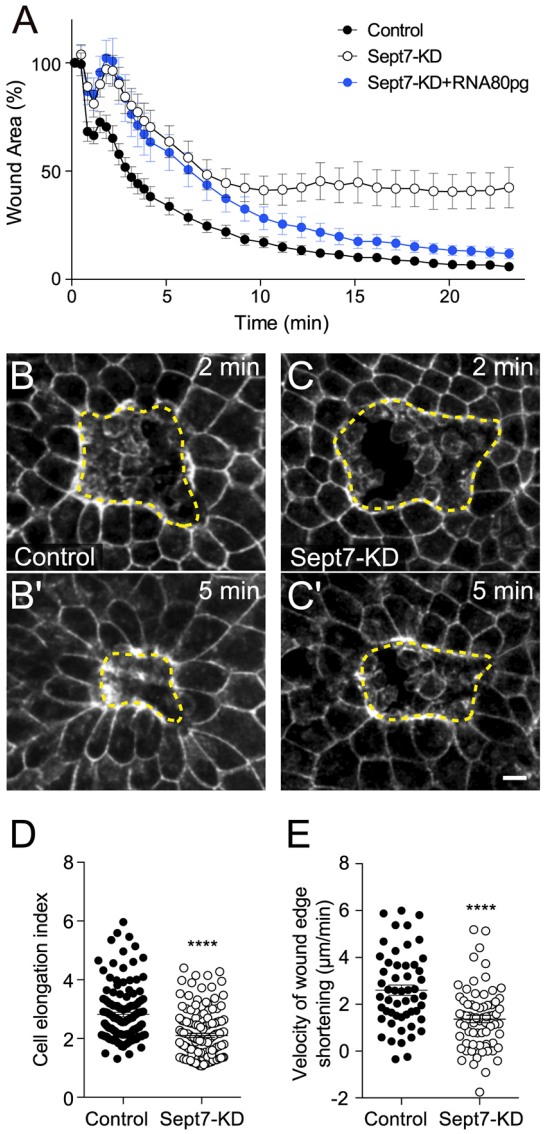

Fig. 4. Sept7 is required for rapid wound closure. (A) Quantification of wound area reduction in control, Sept7-KD and *sept7* mRNA-expressing embryos. The wound area was plotted every 20 s during the first 4 min, and every minute from 4 min onwards after wounding for each group. Control embryos (n=11), Sept7-KD embryos (n=13, 35 ng MO per blastomere), Sept7-KD embryos injected with *sept7* mRNA (80 pg) (n=14) (P<0.0001, two-way ANOVA). (B–C′) Still images from time-lapse imaging of membrane-RFP during wound closure in control embryos (B,B′) and Sept7-KD embryos (C,C′); at 2 min, and at 5 min after wounding. Dotted lines indicate the wound edge. (D) Quantification of cell elongation by measuring ellipticity of each cell surrounding the wound at 15 min after wounding. Control (n=138 from 4 embryos), Sept7-KD embryos (n=136 from 4 embryos). (E) Velocity of cell edge shortening at the wound edge from 2–5 min after wounding in the control (n=53 from 3 embryos) and Sept7-KD embryos (n=71 from 4 embryos). ****P<0.0001, Mann–Whitney *U*-test. Scale bar: 20 µm.

embryos showed attenuated temporal reduction and increased expansion of the wound area during the initial phase; thereafter, the wound size tended to stay the same (Fig. 4A, white circles). Overexpression of *sept7* mRNA was able to rescue the phenotype 10 minutes after wounding of Sept7-KD embryos to that of control embryos (Fig. 4A, blue circles). However, overexpression of the C-terminal deletion mutant (*sept7ΔC*) did not rescue the phenotype in Sept7-KD embryos (Fig. S4), suggesting that septins function as oligomers that are formed by the interaction with their C-terminal coiled-coil domains.

Sept7-KD significantly inhibited cell elongation, with the cells exhibiting low ellipticity at 15 min after wounding (Fig. 4B,B′,D, P<0.0001). Furthermore, the wound edge contraction from 2–5 min after wounding was reduced in Sept7-KD embryos (Fig. 4C,C′,E, P<0.0001). These results suggest that Sept7 is required for inducing rapid cell elongation and wound edge contraction.

Journal of Cell Science (2018) 131, jcs212647. doi:10.1242/jcs.212647

Although we observed a constant delay of wound closure in Sept7-KD embryos, the phenotype associated with slow wound closure was not uniform between embryos [see the higher values of standard error obtained with Sept7-KD embryos compared to those with control embryos (Fig. S5A–C)]. Multiple comparisons of control, Sept7-KD and *sept7* mRNA-expressing embryos revealed a significant difference only at 20 min after wounding, although a tendency to a reversal of the Sept7-KD phenotype was observed in *sept7* mRNA-expressing embryos at all time points. In addition, *sept7* mRNA did not rescue the phenotype observed in the first two minutes, i.e. temporal reduction and expansion of the wound size. Moreover, neither an overdose nor a low dose of injected mRNA disturbed wound closure in control or Sept7-KD embryos (Fig. S5D–F). These results raise the possibility that the amount of Sept7 protein is strictly regulated to function normally for each process or that the regions for Sept7 function are spatially restricted in each cell.

Sept7 and F-actin show associated localization in the intact and wounded epidermis

We next investigated the intracellular localization of Sept7 to determine its relation to the actin cytoskeleton by either using marker protein (Sept7) fused to green fluorescent protein (Sept-GFP) or the F-actin-staining marker Lifeact-RFP (Fig. S6). Sept7-GFP localized at tricellular junctions at a 4–5-µm depth from the apical surface in the intact epidermis and colocalized with the F-actin marker Lifeact-RFP (Fig. S6A). However, higher magnification revealed that the localization of Sept7 was slightly shifted compared to that of F-actin accumulation (Fig. S6B). We therefore quantified the localization pattern by measuring the mean pixel intensity across the tricellular junction (Fig. S6B, yellow line) and the normalized intensities confirmed that Sept7-GFP accumulated next to the F-actin marker (Fig. S6C) but without complete colocalization. The histogram showing the distribution of the distances between each marker revealed that Sept7-GFP was further from the membrane than F-actin (Fig. S6C′, $P<0.0001$, Kolmogorov–Smirnov test).

Observation of Sept7-GFP and F-actin localization during wound closure demonstrated that Sept7-GFP relocalized at the wound edge and along the cell cortices that align radially towards the center of the wound (lateral cell edge, Fig. S6D,E). At the wound edge, Sept7-GFP localized adjacent to the site of F-actin marker accumulation, as observed in the intact epidermis (Fig. S6D,F). These localization patterns suggest that Sept7 has roles both at the wound edge and at the lateral cell cortices during wound closure.

Actomyosin requires Sept7 for function but not for formation at the wound edge

Based on the localization of GFP-Sept7 at the wound edge, we next investigated the role of Sept7 in formation of the actomyosin purse string. We subjected fixed embryos to staining with the actin marker phalloidin and immunostaining for pMLC. Both phalloidin (Fig. S7) and pMLC were detected at the wound edges both in control and Sept7-KD embryos (Fig. 5A,B,C). The ratio of pMLC

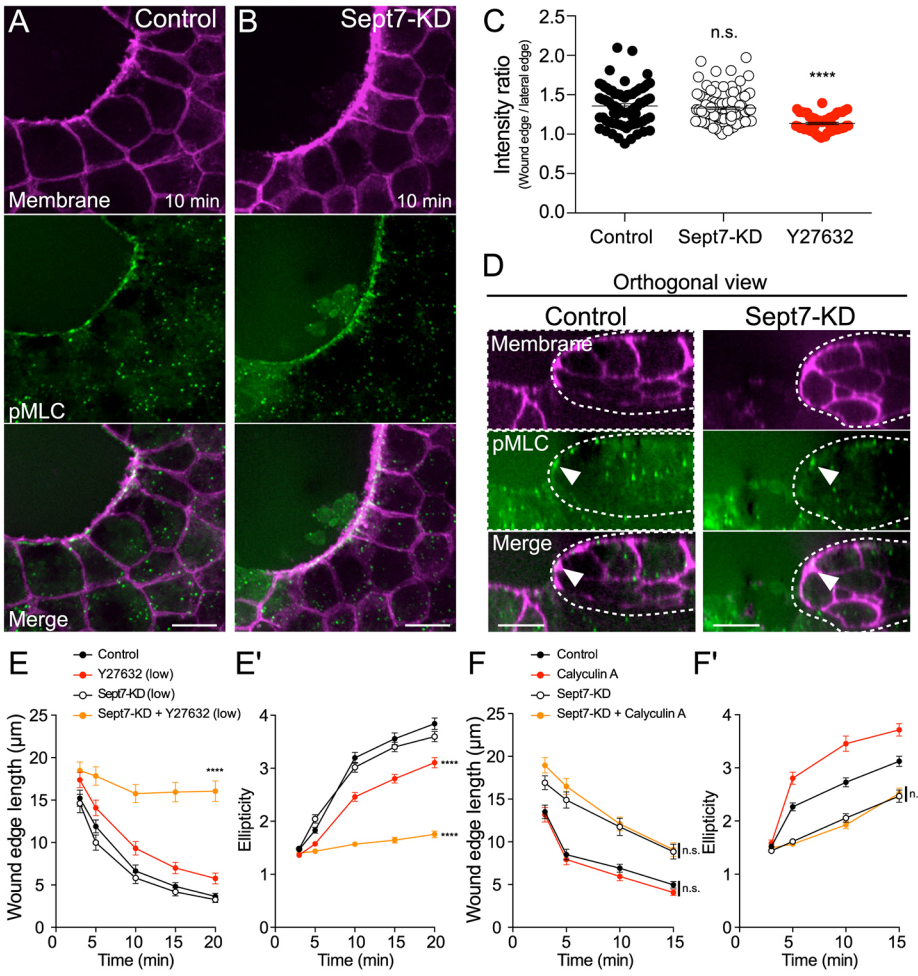

Fig. 5. Actomyosin requires Sept7 for function but not for formation at the wound edge. (A,B) *z*-Projection of the immunostained wound area. Control (A) and Sept7-KD (B) embryos were injected with membrane-GFP and stained with anti-pMLC and anti-GFP antibodies. (C) Quantification of pMLC accumulation at each cell junction along the wound edge, normalized to the mean intensity of lateral cell edge in a cell (Control: $n=76$ from 3 embryos; Sept7-KD: $n=125$ from 4 embryos; Y27632: $n=52$ from 3 embryos). One-way ANOVA followed by the Kruskal–Wallis test for multiple comparisons (****$P<0.0001$). (D) Orthogonal view of the *z*-projection created by using ImageJ. Dotted lines indicate the outer layer closing the wound. Arrowheads indicate the pMLC ring at the wound edge. (E,E′) Quantification of cell edge length at the wound margin and ellipticity of each cell as an index of cell elongation (ellipticity). Two-way ANOVA was followed by Dunnett's test for multiple comparisons. Control: $n=68$ from 3 embryos; Y27632 (low): 20 µM, $n=67$ from 3 embryos; Sept7-KD (low): 17.5 ng MO, $n=57$ from 3 embryos; Sept7-KD+Y27632 (low): $n=54$ from 3 embryos. (F,F′) Same analyses as E and E'. Two-way ANOVA was followed by Tukey's test for multiple comparisons. Control: $n=65$ from 3 embryos; Calyculin A: 125 nM, $n=65$ from 3 embryos; Sept7-KD: 35 ng MO, $n=61$ from 3 embryos; Sept7-KD+Calyculin A: $n=90$ from 4 embryos. Scale bars: 20 µm.

Journal of Cell Science (2018) 131, jcs212647. doi:10.1242/jcs.212647

intensity between the wound edge and lateral cell cortices revealed no significant differences in pMLC accumulation at the wound edge between control and Sept7-KD embryos (Fig. 5C). The ROCK inhibitor Y27632 diminished pMLC staining, suggesting the specificity of the antibody (Fig. 5C). The orthogonal view of z-projection images showed a similar formation of the actomyosin purse string both in control and KD embryos, which is reflected by the pMLC dot at the apical side of the leading edge (Fig. 5D, arrowheads).

Although pMLC immunostaining did not appear to differ between control and Sept7-KD embryos, it is possible that the level of pMLC was insufficient to trigger the contractile forces in the knockdown embryos. Consistent with this conjecture, treatment with a lesser amount (20 µM) of Y27632 in combination with half the dose of Sept7 morpholino (17.5 ng per blastomere) showed synergistic effects with regard to cell elongation and wound edge shortening, suggesting that Sept7 functions together with ROCK to contract the wound edges (Fig. 5E,E′). We then attempted to rescue the phenotype by treatment with calyculin A (Caly A), an inhibitor of myosin phosphatase that causes continuous phosphorylation of myosin light chains. However, Caly A failed to rescue the Sept7-KD phonotypes including less cell elongation and wound edge contraction (Fig. 5F,F′). Notably, Caly A treatment of control embryos resulted in increased cell elongation (Fig. 5F′), indicating that the inhibitor penetrates the embryo and functions at this concentration. Therefore, together with the results shown in Fig. 4, these findings demonstrate that Sept7 is required for actomyosin to generate functional contractile forces but not for formation of the actomyosin purse string.

Sept7 coordinates microtubule reorientation after wounding

We next investigated the localization of the microtubule bundles that were observed in Fig. 2. Immunostaining of α-tubulin revealed that the surrounding cells established tubulin bundles along the vertical cell cortices at a depth of 4–5-µm from the apical surface (Fig. 6A,B). However, the cortical microtubules were not clearly visible in Sept7-KD embryos (Fig. 6C,D).

To quantify the microtubule phenotypes in Sept7-KD embryos, we generated a profile plot of pixel intensities across the ∼4-µm-long lateral cell cortices (Fig. 6E), as for the analysis shown in Fig. S6. We detected three patterns of cortical microtubule accumulation: single, double or triple peaks both in control and Sept7-KD embryos (Fig. 6F, green line). The number of peaks and the interpeak distance reflect the cohesiveness of microtubule filaments and the cell membrane, with more peaks or longer interpeak distance indicating less cohesion. Sept7-KD embryos appeared to exhibit more double and triple peaks of α-tubulin than control embryos (Fig. 6G). Furthermore, the distance between the

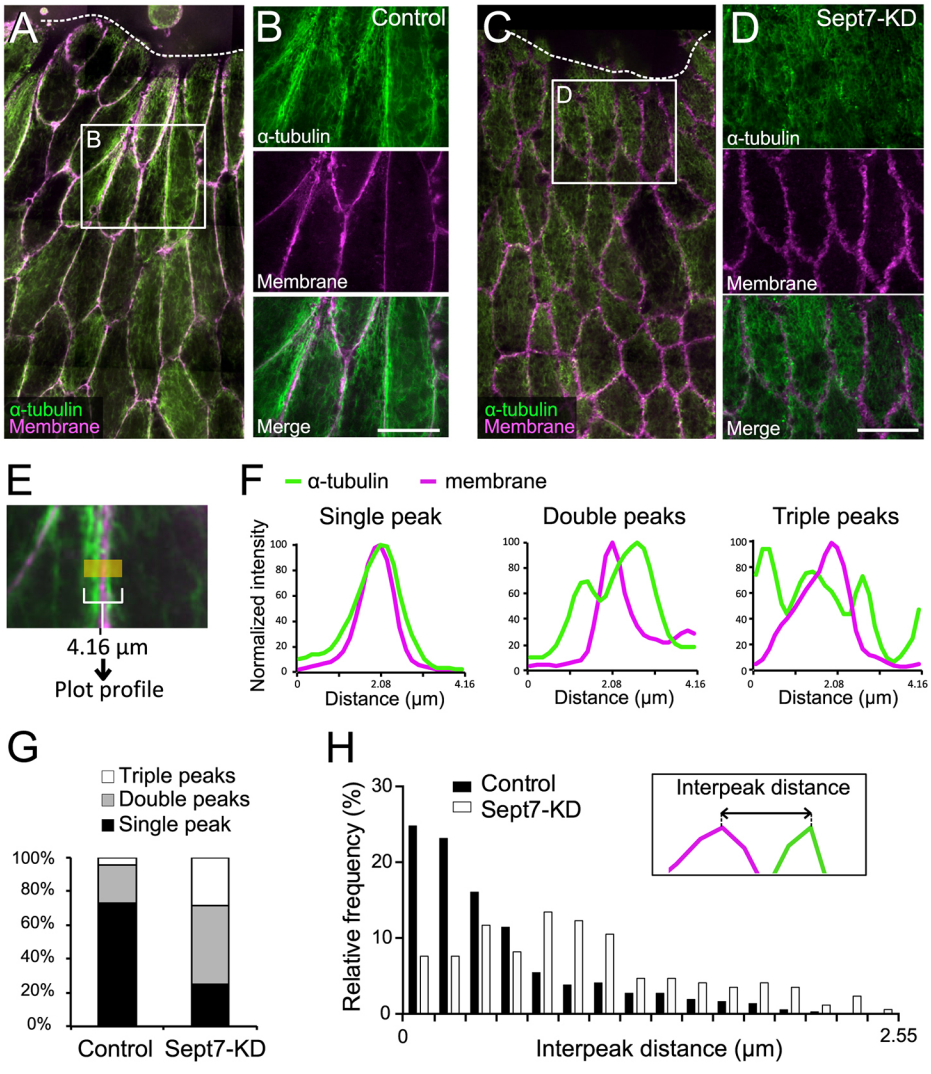

Fig. 6. Sept7 coordinates microtubule reorientation after wounding. (A–D) Immunostaining of α-tubulin (green) for microtubules and GFP (magenta) for the membrane. Control or Sept7-KD embryos were fixed 15 min after wounding. Dotted lines indicate the wounded edge; boxed areas in A and C are shown magnified in B and D, respectively; scale bars: 20 µm. (E) Pixel intensities of α-tubulin and the membrane measured on the yellow line drawn across the vertical cell membrane. Pixel intensities were used to create the profile plot in F. (F) Patterns of profile plots of α-tubulin and the membrane. Single, double or triple peaks of α-tubulin reflect cohesiveness of microtubule filaments and the cell membrane. (G) Relative frequency of the three patterns of profile plots shown in F. (H) Histogram showing the distribution of the distance between the peaks (interpeak distance) of α-tubulin and membrane in the profile plots. Control: *n*=367; KD: *n*=171; *n*=2 embryos per group. Range of each bin is 0.16 µm. Data were analyzed using the Kolmogorov-Smirnov test ($P<0.0001$).

Journal of Cell Science (2018) 131, jcs212647. doi:10.1242/jcs.212647

peaks of cell membrane and α-tubulin was less in control embryos and more widely dispersed in Sept7-KD embryos (Fig. 6H, $P<0.0001$, Kolmogorov–Smirnov test). These data suggest that Sept7 is required for reorganization of the microtubules in order to attach to the lateral cell membrane during wound closure.

Sept7 controls the interaction between microtubules and the cell membrane independently from microtubule stabilization

We further investigated the function of Sept7 for microtubule reorganization along the lateral cell cortices. The observation that there are fewer microtubule bundles along the cell membrane in Sept7-KD embryos (Fig. 6C) raised the possibility that the post-translational modification of tubulin associated with microtubule stabilization is affected by depletion of Sept7. Based on this speculation, we artificially induced stabilized microtubules by overexpressing *map7* (ensconsin) mRNA, which has been shown to cause tubulin acetylation (Masson and Kreis, 1993).

We confirmed faint staining of acetylated (Ac) α-tubulin in the intact epidermis of control and Sept7-KD embryos (Fig. S8A,B). Overexpression of GFP-tagged Map7 protein (Map7-GFP) (Brooks and Wallingford, 2015) in the epidermis successfully increased thick microtubule filaments, as seen by staining for Ac-α-tubulin in both control and Sept7-KD embryos (Fig. S8C,D). Sept7-KD embryos had aster-like microtubule organization (Fig. S8D); however, we noticed that the thick bundles along cell–cell junctions did not attach tightly to the cell membrane in Sept7-KD embryos (Fig. S8E,F). Quantification of the distance between Ac-microtubules and cell–cell junctions further revealed localization of Ac-microtubule filaments distinct from cell–cell junctions in Sept7-KD embryos (Fig. S8G).

Similar results were obtained from cells closing the wound (Fig. 7A,B), wherein the induced Ac-microtubule was detached from the cell–cell junction in the Sept7-KD embryos at 15 min after wounding (Fig. 7C,D). Plot profile analysis to quantify the position of the cortical Ac-microtubules relative to the cell–cell junction demonstrated that Sept7-KD embryos show a greater frequency of double or triple peaks of Ac-α-tubulin intensity (Figs 6F and 7E). The histogram of the distribution of the distance between the cell–cell junction and Ac-α-tubulin confirmed that Ac-microtubules were detached from the cell–cell junction in knockdown embryos (Fig. 7F). Notably, *map7* overexpression did not rescue the slow wound closure caused by Sept7-KD (Fig. S8H). These results suggest that stabilization or acetylation of the microtubule alone is not sufficient to localize the microtubule filaments at the cell cortices and that formation of stabilized microtubule bundles is unlikely to constitute the objective of Sept7 function during wound closure.

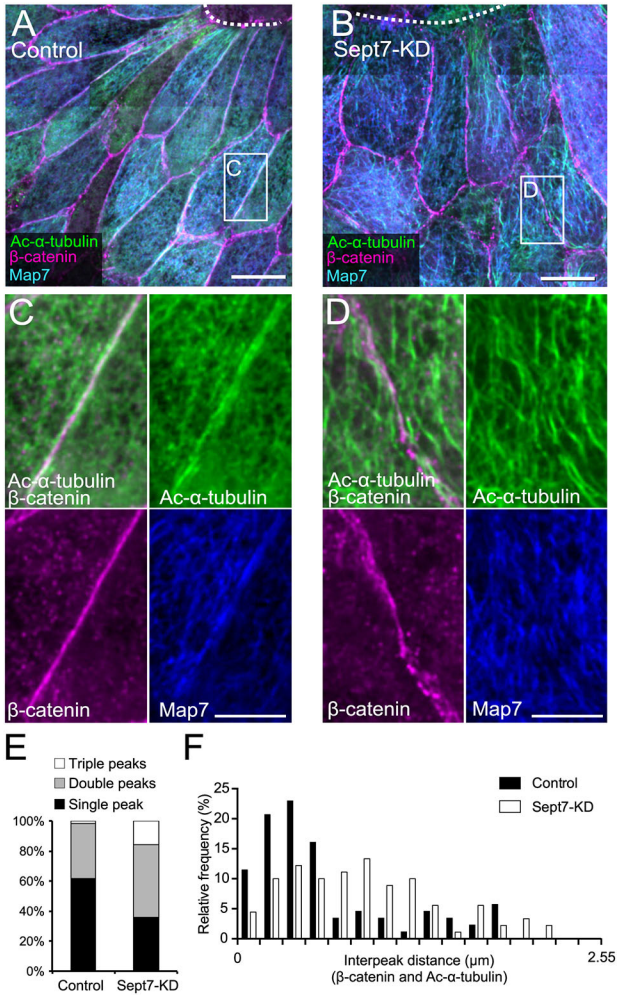

Fig. 7. Sept7 controls microtubule reorientation independently from microtubule stabilization. (A–D) Immunostaining of acetylated α-tubulin (Ac-α-tubulin) in stabilized microtubules, of β-catenin in the cell–cell junction and of GFP in cells overexpressing Map7-GFP. Images in A and B are tile scanned, boxed areas in A and B are shown magnified in C and D, respectively; scale bars: 20 µm (A,B), 10 µm (C,D). (E) Relative frequency of three patterns of plot profiles of Ac-α-tubulin. Analyses are the same as those described for Fig. 4E–G. (F) Histogram showing the distribution of the distance between the intensity peaks of Ac-α-tubulin and β-catenin in the profile plot. Control: $n=87$; KD: $n=90$, from 2 embryos per group. Range of each bin is 0.16 µm. Data was analyzed using the Kolmogorov-Smirnov test ($P<0.0001$).

Septins and microtubules functionally interact to effect wound closure

We next investigated potential functional interactions between septins and microtubules during wound closure. Here, Sept7 knockdown – obtained with 50% of morpholino (17.5 ng per blastomere) compared to that usually utilized in knockdown experiments – was weak; embryos were then treated with a 25% of nocodazole (5 µM) compared to that applied previously. Single treatment of either morpholino or nocodazole had only a slight effect on cell elongation at the wound edge (Fig. 8A–C,E). In contrast, combination of both interfered with cell elongation in an additive manner (Fig. 8D,E). We found that 3 minutes after wounding the length of the cell edge at the wound margin – which was longer in nocodazole-treated embryos (see Fig. 2) –was also increased in embryos treated with both low dose nocodazole and morpholino (Fig. 8F). The velocity of wound edge contraction did not show significant difference between the groups (Fig. 8G). Elongation of the lateral edge, however, was significantly less in embryos treated with nocodazole and morpholino together (Fig. 8H), and was specifically altered by the nocodazole treatment (see Fig. 2). These results suggest that Sept7 works together with or requires microtubules to function normally during wound closure.

DISCUSSION

Our study demonstrates a contribution of microtubules and septins to the cellular behaviors for multi-cellular wound closure in the vertebrate embryo, revealing a cooperating role of the cytoskeleton including the actomyosin purse string. Microtubule reorganization after wounding appears to be crucial to control the initial length of the cell edge at wound margin as well as cell elongation, both of which are necessary for rapid wound closure. Specifically, by using a Sept7-KD

Journal of Cell Science (2018) 131, jcs212647. doi:10.1242/jcs.212647

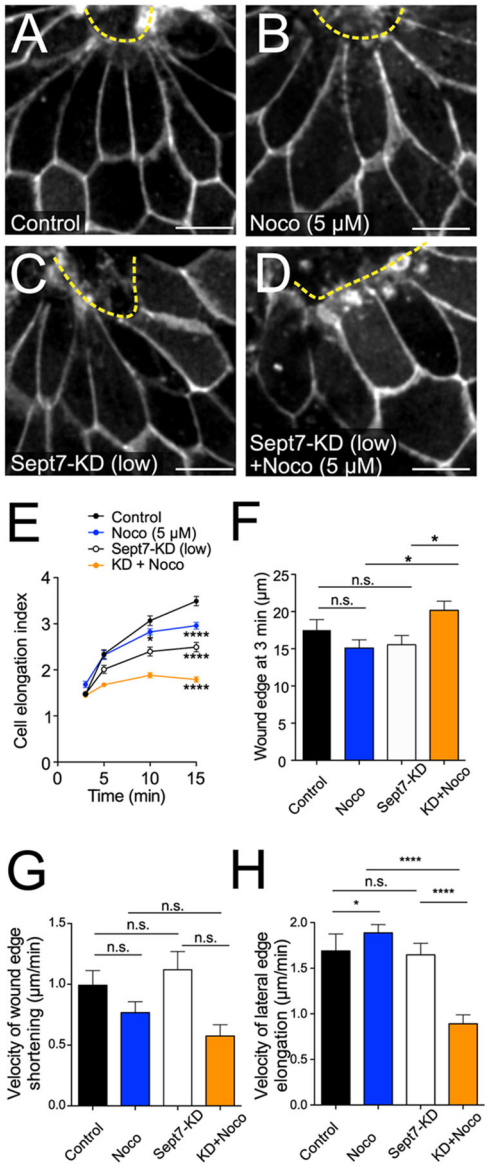

Fig. 8. Sept7 and microtubules functionally interact during wound closure. (A–D) Live imaging of cell shape in the wounded epidermis of the embryos at 15 min after wounding. Embryos were co-injected with membrane-BFP and α-tubulin-emerald GFP to confirm the effects of nocodazole (Noco). Images show only membrane BFP (white). Embryos were treated with DMSO as control (A), a low concentration (5 µM) of nocodazole (B), weak knockdown of Sept7 (17.5 ng MO) (C) and the combination of weak Sept7 knockdown and low concentration of nocodazole (D). Dotted lines indicate the wound edge. Scale bars: 20 µm.
(E) Quantification of cell elongation by measuring the ellipticity of each cell attached to the wound. *P=0.0444, ****P<0.0001, two-way ANOVA followed by Dunnett's test for multiple comparisons. Control: n=60 from 3 embryos; Noco (5 µM): n=74 from 4 embryos; Sept7-KD (17.5 ng of MO): n=57 from 4 embryos; KD+Noco (17.5 ng MO+5 µM nocodazole): n=71 from 4 embryos. (F) Average comparison of wound edge length in each cell at 3 minutes after wounding. *P=0.0284 (nocodazole versus nocodazole+Sept7-MO). *P=0.0421 (Sept7-KD versus nocodazole+Sept7-KD). One-way ANOVA followed by Kruskal–Wallis test for multiple comparisons. (Control: n=39 from 3 embryos, nocodazole: n=54 from 3 embryos, sept7-MO: n=49 from 3 embryos, Sept7-KD+nocodazole: n=54 from 3 embryos). (G,H) Average comparisons of velocity of wound edge shortening (G) or lateral edge elongation (H) at 3–10 min after wounding. *P=0.0468, ***P<0.0001; one-way ANOVA followed by Kruskal–Wallis test for multiple comparisons, (Control: n=35 from 3 embryos, nocodazole: n=42 from 3 embryos, Sept7-KD: n=38 from 3 embryos, Sept7-KD+nocodazole: n=58 from 4 embryos).

X. laevis embryo model, we showed that knockdown of Sept7 resulted in microtubule disorganization, attenuating cell elongation.

Our findings reinforce the significance of the microtubule for wound closure and expand the role of septins therein. Previously, the necessity of microtubules for wound closure was suggested through studies of *X. laevis* oocytes and *D. melanogaster* embryos that focused on the function of the actomyosin purse string (Mandato and Bement, 2003; Abreu-Blanco et al., 2012). For instance, microtubules were shown to transport actin to the wound edge as observed in single-cell wound healing. However, as the actomyosin purse string was considered to constitute a main force in driving wound closure, the specific microtubule-associated cellular behaviors during wound closure remained to be elucidated. By taking advantage of the large cells in *X. laevis* embryos, which allow imaging using high-speed confocal microscopy, we captured this microtubule rearrangement and its significance during wound closure. It should be noted that microtubule rearrangement does not always follow a change in cell shape during collective cell movement– as previously observed by us in tissue undergoing convergent extension (Shindo et al., 2008). Indeed, our results in response to specifically inhibiting either microtubules or actomyosin raise the possibility that microtubules can elongate the lateral cell edges, which align perpendicularly to the wound edge. Notably, Sept2 has previously been reported to directly bind to microtubules or microtubule-binding proteins and to guide microtubules in order to generate correct alignment (Bowen et al., 2011; Nölke et al., 2016). In addition, Sept9 is known to function in the bundling of microtubule filaments (Bai et al., 2013). Although the off-target effect of morpholinos is a potential concern, our results add another association between septins and microtubules in multi-cellular events *in vivo* by indicating that the microtubule is required for rapid cell elongation and wound edge contraction in cooperation with septins.

Although we have demonstrated that septins and microtubules have a substantial role in embryonic wound closure, the specific mechanism by which septins regulate microtubules remains unclear. It is possible that septins act as linkers to connect microtubules to the cell membrane; indeed, septins have been shown to facilitate the interaction of the phospholipid membrane and microtubules (Bertin et al., 2010; Nagata et al., 2003). Another possible mechanism is through post-translational modification. Sept7 has previously shown to provide a scaffold for histone deacetylase 6, allowing efficient microtubule deacetylation during neurite growth (Ageta-Ishihara et al., 2013). In addition, septin knockdown was found to increase the acetylation of microtubules by inducing extra binding of Map4 (Kremer et al., 2005). In contrast, our present findings suggest the opposite effect of Sept7 on microtubule acetylation. We did not observe hyperacetylation in Sept7-KD embryos, which – instead – showed filaments thinner than those in controls. Furthermore, we failed to rescue wound closure defects, or to cause additive defects in Sept7-KD embryos by inducing acetylated microtubules. Because cell movement during wound closure occurs more rapidly than other physiological events, specialized cytoskeletal interactions might be established. Further investigations of wound-specific triggers, e.g. damage signals (Cordeiro and Jacinto, 2013), would provide a better understanding of the distinct role of septins in microtubule regulation during wound closure.

Our results clearly show that embryonic wounds are closed not only by wound edge contraction but also by rapid cell elongation. Although the involvement of septins in mammalian wound closure has not yet been established, we demonstrate that the rapid cell elongation during wound closure is conserved in mammalian embryos. The actomyosin purse string has been well studied as a force driving wound edge contraction; however, the driving forces of rapid cell elongation had

not been previously clarified. Notably, our data indicate that – on its own – inhibition of actomyosin contraction, microtubule polymerization or Sept7 expression does not completely suppress cell elongation. Thus, the overlapping roles between actomyosin, microtubules and septins can elongate cells and facilitate rapid wound closure. Such coordination of cytoskeletal components might be crucial to cause exclusive and rapid cellular behaviors during wound closure, compared with the less fast collective cell movements during morphogenesis. For example, neural tube closure in *X. laevis* (Suzuki et al., 2017) and convergent germband extension in *D. melanogaster* (Levayer and Lecuit, 2013; Yu and Fernandez-Gonzalez, 2016) comprise relatively slower cell movements than wound closure that occurs together with oscillation of actomyosin, a phenomenon that was not detected during wound closure imaged at the same time-lapse intervals (data not shown). Our findings, thus, raises the question how the combination of cytoskeleton components contributes to the generation of several modes of actomyosin contractility during collective cell movement *in vivo*.

It remains unknown how Sept7 regulates actomyosin contractility. We observed Sept7-GFP localization at the wound edge but did not detect abnormal formation of the actomyosin purse string upon Sept7 depletion visible by using confocal microscopy. However, whereas our pharmacological analyses showed that Sept7 can functionally interact with actomyosin, the phenotypes were not rescued when was contractility enhanced (Fig. 5). One explanation of this apparent inconsistency is that contractile forces of actomyosin without Sept7 cannot be transmitted physically to the cell membrane. For example, we have previously shown that Sept7 functions as a partition protein for F-actin at the multicellular junctions in the mesoderm tissue (Shindo and Wallingford, 2014). Such localization of septins associated with F-actin was observed in various experimental systems, including during cytokinesis and neuronal blanching (Xie et al., 2007; Hu et al., 2012). Our observation of Sept7-GFP in the intact tissue is reminiscent of the conserved function of septins. Therefore, we cannot rule out the possibility that the actomyosin purse string is functionally disturbed in Sept7-KD embryos, in a manner that cannot be detected by using confocal microscopy. Further analysis using super-resolution microscopy or investigation of, for example, the role of junctional proteins, such as cadherin (Hunter et al., 2015), might help to address this issue.

In summary, we have demonstrated that septins play a functional role in organizing the microtubules and actomyosin purse string during embryonic wound closure. Our results provide new insight into the diversity of the crosstalk between cytoskeletal components during dynamic cell movements *in vivo*, highlighting a marked resilience of embryos against wounding.

MATERIALS AND METHODS

X. laevis embryo preparation and microinjection

Ovulation in female adult *X. laevis* was induced by injection of human chorionic gonadotropin. After overnight incubation, the eggs were harvested by squeezing the female frog, fertilized *in vitro* and dejellied in 3% cysteine (pH 7.8) solution at the two-cell stage. Embryos were then washed and subsequently reared in ×1/3 Marc's modified Ringer's (MMR) solution. For microinjections, when reaching the four-cell stage, the embryos were placed in 3% Ficoll in ×1/3 MMR solution, injected using a glass capillary and microinjector (Narishige IM300), and then reared in 3% Ficoll solution until reaching the appropriate stages for analysis.

Preparations of plasmids and mRNA for live imaging, and morpholino antisense oligonucleotides

The open reading frame of the human α-tubulin gene fused to an Emerald GFP construct was a gift from Dr Yuko Mimori-Kiyosue (RIKEN) and subcloned into the pCS10R plasmid (Kieserman et al., 2010). Lifeact-GFP and Lifeact-RFP were a gift from Dr Noriyuki Kinoshita (NIBB). The N-terminal open reading frame of the *Xenopus* sept7 gene (1–349AA) was amplified from extracted cDNA to generate sept7ΔC plasmid (Fig. S4), and inserted into the pCS10R vector. Capped mRNA was synthesized using the mMESSAGE mMACHINE kit (Ambion). The following amounts of mRNAs were injected into ventral blastomeres of *X. laevis* embryos at the four-cell stage to target the epidermis: 60 pg α-tubulin-emerald GFP to label α-tubulin, 60 pg membrane-GFP, 60 pg membrane-RFP, 60 pg membrane-BFP (farnesylation sequence) (Megason and Fraser, 2003; Gong et al., 2004) and 60 pg Lifeact-RFP to label F-actin (Suzuki et al., 2017). 80 pg map7-GFP was injected to stabilize microtubules. The Sept7 morpholino has been described previously (Kim et al., 2010; Shindo and Wallingford, 2014).

Stereoscope imaging

X. laevis embryos were incubated until stage 13. After removal of the vitelline membrane, the embryo was wounded by by cutting out a small piece of the outermost epidermal layer using forceps or a glass capillary while placing the embryo in 1.5–2× Steinberg's solution.

Live imaging of *X. laevis* embryos

After the blastopore was completely closed (around stage 12.5), the vitelline membrane of injected *X. laevis* embryos was removed using forceps. Each embryo was mounted to a glass-bottom dish in 1.5–2× Steinberg's solution. To fix the position on the dish, the embryo was pressed down gently using a coverslip with silicon grease placed in between to avoid squishing. For the wounding experiment, the embryo was then mounted on the dish with the wounded side facing down. Live imaging was performed using a Yokogawa Cell Voyager CV1000 Confocal Scanner Box (Yokogawa Electric).

Immunostaining and antibodies

For *X. laevis* α-tubulin and acetylated α-tubulin staining, the embryos were fixed using modified low-FG fixation reagent (Kofron et al., 2002; Wühr et al., 2010) [0.5% formaldehyde and 0.1% glutaraldehyde in phosphate-buffered saline (PBS)] at room temperature (22–26°C) for 0.5–1 h. For detection of phosphorylated myosin light chain, embryos were fixed using 2% trichloroacetic acid as described in Nandadasa et al. (2009). *X. laevis* embryos were incubated with the following primary antibodies at 4°C overnight: mouse anti-acetylated-α-tubulin antibody (1:300 dilution, T7451, Sigma-Aldrich), mouse anti-α-tubulin (1:400, T9026, Sigma-Aldrich), rabbit anti-β-catenin (1:300, ab2365, Abcam), chick anti-GFP (1:500, ab13970, Abcam), rabbit anti-phosphorylated myosin light chain 2 (pMLC; 1:150, ab2480, Abcam) and mouse anti-myosin light chain 9 (1:150, MA5-15163, Thermo Fisher Scientific). After primary antibody incubation, all samples were first washed and subsequently treated with the following secondary antibodies for 2 h at room temperature: Alexa Fluor 488 goat anti-mouse IgG (H+L) (1:300, A-11029, Thermo Fisher), Alexa Fluor 555 goat anti-rabbit (1:500, A-11008, Thermo Fisher) and Alexa Fluor 405 goat anti-chicken (1:1000, ab175674, Abcam). All samples were then washed with PBST (PBS with 0.03% Triton X-100) and stored in fresh PBST at 4°C until imaging with the CV1000 scanner.

For mouse phalloidin and wheat germ agglutinin (WGA) staining, wounded mouse embryos were fixed with 4% paraformaldehyde for 1 h. After washing in PBST (PBS with 0.05% Triton X-100), whole-mounted embryos were stained with Alexa Fluor 488-conjugated phalloidin (1:500, A12379, Thermo Fisher) and 647-conjugated WGA (1:500, W32466, Thermo Fisher) at 4°C overnight.

Wounding of *X. laevis* embryos

The outer layer of epidermis at the lateral surface of *X. laevis* neurula embryos (stage 13–18) was peeled off using sharp forceps or removed by aspiration with a glass capillary using a microinjector. A total of 20–30 cells of the outer layer were removed (circular shape ∼100 µm in diameter, ∼8500 µm^2) under the stereomicroscope. Time-lapse images were then captured using either stereoscopy or confocal microscopy.

Wounding of mouse embryos

All mouse experiments were approved by the Animal Care and Use Committee of Nagoya University Graduate School of Medicine. Pregnant C57/BL/6J mice were purchased from Japan SLC (Shizuoka, Japan). Dams were killed under deep anesthesia when embryos had reached embryonic day 9 (E9). After isolation of an embryo, its left lateral epidermis was wounded with a sewing needle. The wounded embryo was incubated in the embryonic medium (DMEM, 50% rat serum, 10 µM MEM-non-essential amino acids, and 1 mM 2-mercaptoethanol) at 37°C for 5 or 20 min. The wound was ∼100-µm in diameter within 5 min after wounding, and was 30–50 µm in diameter within 20 min after wounding.

Inhibitor treatment

To interfere with the polymerization of microtubules, embryos were treated with nocodazole. The treated and untreated (control) embryos were placed in 20 or 5 µM nocodazole or, as a control, the same amount of dimethyl sulfoxide (DMSO) for 1.5–2 h or 45 min before wounding, respectively. The Rho-associated kinase inhibitor Y27632 (20 or 50 µM) or Calyculin A (125 nM) was applied to the embryo for 3–5 min prior to imaging.

Image analyses and statistical analysis

Images were quantified by using Fiji (https://fiji.sc/). Prism 6.0 (GraphPad Software) and Excel (Microsoft) was used for statistical analyses. Wound area measurements, cell elongation and wound edge shortening were analyzed by two-way analysis of variance (ANOVA, followed by Dunnett's test or Tukey's test). The histograms for the distribution of distance (Fig. 6H and 7F, Figs S6C′ and S8G) were analyzed using the Kolmogorov–Smirnov test. For the other data, Student's t-test (Fig. 3D), Mann–Whitney U-test (Figs 3E; 4D,E; Figs S1C,D; S7C) and one-way ANOVA followed by the Kruskal–Wallis test (Figs 1D,E; 2G–I; 5C; 8F; Figs S2D; S4) were applied. Error bars indicate ±s.e.m. When sample numbers differed greatly between the compared groups, random sampling was performed by using software from the free software environment R (https://www.r-project.org/).

Acknowledgements

We thank Victoria Le for technical assistance. We also thank Keita Ohsumi, Mariko Iwabuchi and Tomoko Nishiyama for sharing the frog facility.

Competing interests

The authors declare no competing or financial interests.

Author contributions

Conceptualization: A.S., J.B.W., M.K.; Methodology: A.S., J.B.W., M.K.; Validation: A.S., A.A., M. Takagishi; Formal analysis: A.S.; Investigation: A.S., A.A., M. Takagishi; Resources: A.S., M. Takahashi, J.B.W., M.K.; Data curation: A.S., A.A., M. Takagishi; Writing - original draft: A.S.; Writing - review & editing: A.S., A.A., J.B.W., M.K.; Visualization: A.S.; Supervision: A.S., J.B.W., M.K.; Project administration: A.S., J.B.W., M.K.; Funding acquisition: A.S., M. Takahashi, J.B.W., M.K.

Funding

This work is supported by grants from Japan Society for the Promotion of Science (grant numbers: JP15H01318, JP15K21065, JP26891012 and JP17K17799), the Sumitomo Foundation, the Hori Sciences & Arts Foundation, the Public Foundation of Chubu Science and Technology Center, the Tomizawa Jun-ichi & Keiko Fund of Molecular Biology Society of Japan for Young Scientists, and the Adaptable and Seamless Technology Transfer Program through Target-driven R&D from the Japan Science and Technology Agency (grant number: J5416) to A.S. Work in M.K.'s lab is supported by JSPS KAKENHI. Work in J.B.W.'s lab was supported by the National Institutes of Health (National Institute of General Medical Science and National Heart, Lung, and Blood Institute) to J.B.W., and a Kanae Foundation grant for the promotion of medical science to A.S. A.S. and M. Takagishi. were supported by the Program for Promoting the Enhancement of Research Universities, as a Young researcher unit for the advancement of new and undeveloped fields in Nagoya University. Deposited in PMC for release after 12 months.

Supplementary information

Supplementary information available online at
http://jcs.biologists.org/lookup/doi/10.1242/jcs.212647.supplemental

References

Abreu-Blanco, M. T., Verboon, J. M. and Parkhurst, S. M. (2011). Cell wound repair in Drosophila occurs through three distinct phases of membrane and cytoskeletal remodeling. *J. Cell Biol.* **193**, 455-464.

Abreu-Blanco, M. T., Verboon, J. M., Liu, R., Watts, J. J. and Parkhurst, S. M. (2012). Drosophila embryos close epithelial wounds using a combination of cellular protrusions and an actomyosin purse string. *J. Cell Sci.* **125**, 5984-5997.

Ageta-Ishihara, N., Miyata, T., Ohshima, C., Watanabe, M., Sato, Y., Hamamura, Y., Higashiyama, T., Mazitschek, R., Bito, H. and Kinoshita, M. (2013). Septins promote dendrite and axon development by negatively regulating microtubule stability via HDAC6-mediated deacetylation. *Nat. Commun.* **4**, 2532.

Bai, X., Bowen, J. R., Knox, T. K., Zhou, K., Pendziwiat, M., Kuhlenbäumer, G., Sindelar, C. V. and Spiliotis, E. T. (2013). Novel septin 9 repeat motifs altered in neuralgic amyotrophy bind and bundle microtubules. *J. Cell Biol.* **203**, 895-905.

Bement, W. M., Mandato, C. A. and Kirsch, M. N. (1999). Wound-induced assembly and closure of an actomyosin purse string in Xenopus oocytes. *Curr. Biol.* **9**, 579-587.

Bertin, A., McMurray, M. A., Thai, L., Garcia, G.III, Votin, V., Grob, P., Allyn, T., Thorner, J. and Nogales, E. (2010). Phosphatidylinositol-4, 5- bis phosphate promotes budding yeast septin filament assembly and organization. *J. Mol. Biol.* **404**, 711-731.

Bowen, J. R., Hwang, D., Bai, X., Roy, D. and Spiliotis, E. T. (2011). Septin GTPases spatially guide microtubule organization and plus end dynamics in polarizing epithelia. *J. Cell Biol.* **194**, 187-197.

Brock, J., Midwinter, K., Lewis, J. and Martin, P. (1996). Healing of incisional wounds in the embryonic chick wing bud: characterization of the actin purse-string and demonstration of a requirement for Rho activation. *J. Cell Biol.* **135**, 1097-1107.

Brock, A. R., Wang, Y., Berger, S., Renkawitz-Pohl, R., Han, V. C., Wu, Y. and Galko, M. J. (2012). Transcriptional regulation of Profilin during wound closure in Drosophila larvae. *J. Cell Sci.* **125**, 5667-5676.

Brooks, E. R. and Wallingford, J. B. (2015). In vivo investigation of cilia structure and function using Xenopus. *Methods Cell Biol.* **127**, 131-159.

Cordeiro, J. V. and Jacinto, A. (2013). The role of transcription-independent damage signals in the initiation of epithelial wound healing. *Nat. Rev. Mol. Cell Biol.* **14**, 249-262.

Davidson, L. A., Ezin, A. M. and Keller, R. (2002). Embryonic wound healing by apical contraction and ingression in Xenopus laevis. *Cell Motil. Cytoskeleton* **53**, 163-176.

Gong, Y., Mo, C. and Fraser, S. E. (2004). Planar cell polarity signalling controls cell division orientation during zebrafish gastrulation. *Nature* **430**, 689-693.

Haigo, S. L., Hildebrand, J. D., Harland, R. M. and Wallingford, J. B. (2003). Shroom induces apical constriction and is required for hingepoint formation during neural tube closure. *Curr. Biol.* **13**, 2125-2137.

Hu, J., Bai, X., Bowen, J. R., Dolat, L., Korobova, F., Yu, W., Baas, P. W., Svitkina, T., Gallo, G. and Spiliotis, E. T. (2012). Septin-driven coordination of actin and microtubule remodeling regulates the collateral branching of axons. *Curr. Biol.* **22**, 1109-1115.

Hunter, M. V., Lee, D. M., Harris, T. J. C. and Fernandez-Gonzalez, R. (2015). Polarized E-cadherin endocytosis directs actomyosin remodeling during embryonic wound repair. *J. Cell Biol.* **210**, 801-816.

Joo, E., Surka, M. C. and Trimble, W. S. (2007). Mammalian SEPT2 is required for scaffolding nonmuscle myosin II and its kinases. *Dev. Cell* **13**, 677-690.

Kieserman, E. K., Lee, C., Gray, R. S., Park, T. J. and Wallingford, J. B. (2010). High-magnification in vivo imaging of Xenopus embryos for cell and developmental biology. *Cold Spring Harb. Protoc.* **2010**, pdb.prot5427.

Kim, S. K., Shindo, A., Park, T. J., Oh, E. C., Ghosh, S., Gray, R. S., Lewis, R. A., Johnson, C. A., Attie-Bittach, T., Katsanis, N. et al. (2010). Planar cell polarity acts through septins to control collective cell movement and ciliogenesis. *Science* **329**, 1337-1340.

Kinoshita, M., Kumar, S., Mizoguchi, A., Ide, C., Kinoshita, A., Haraguchi, T., Hiraoka, Y. and Noda, M. (1997). Nedd5, a mammalian septin, is a novel cytoskeletal component interacting with actin-based structures. *Genes Dev.* **11**, 1535-1547.

Kofron, M., Heasman, J., Lang, S. A. and Wylie, C. C. (2002). Plakoglobin is required for maintenance of the cortical actin skeleton in early Xenopus embryos and for cdc42-mediated wound healing. *J. Cell Biol.* **158**, 695-708.

Kremer, B. E., Haystead, T. and Macara, I. G. (2005). Mammalian septins regulate microtubule stability through interaction with the microtubule-binding protein. *Mol. Biol. Cell* **16**, 4648-4659.

Lawson, A. and England, M. A. (1998). Surface ectodermal wound healing in the chick embryo. *J. Anat.* **192**, 497-506.

Lee, J.-Y. (2012). Uncorking gastrulation: the morphogenetic movement of bottle cells. *Wiley Interdiscip. Rev. Dev. Biol.* **1**, 286-293.

Levayer, R. and Lecuit, T. (2013). Oscillation and polarity of E-cadherin asymmetries control actomyosin flow patterns during morphogenesis. *Dev. Cell* **26**, 162-175.

Mandato, C. A. and Bement, W. M. (2003). Actomyosin transports microtubules and microtubules control actomyosin recruitment during Xenopus oocyte wound healing. *Curr. Biol.* **13**, 1096-1105.

Martin, P. (1997). Wound healing-aiming for perfect skin regeneration. *Science* **276**, 75-81.
Martin, P. and Lewis, J. (1992). Actin cables and epidermal movement in embryonic wound healing. *Nature* **360**, 179-183.
Masson, D. and Kreis, T. E. (1993). Identification and molecular characterization of E-MAP-115, a novel microtubule-associated protein predominantly expressed in epithelial cells. *J. Cell Biol.* **123**, 357-371.
McCluskey, J. and Martin, P. (1995). Analysis of the tissue movements of embryonic wound healing–DiI studies in the limb bud stage mouse embryo. *Dev. Biol.* **170**, 102-114.
Megason, S. G. and Fraser, S. E. (2003). Digitizing life at the level of the cell: high-performance laser-scanning microscopy and image analysis for in toto imaging of development. *Mech. Dev.* **120**, 1407-1420.
Mostowy, S. and Cossart, P. (2012). Septins: the fourth component of the cytoskeleton. *Nat. Rev. Mol. Cell Biol.* **13**, 183-194.
Nagata, K., Kawajiri, A., Matsui, S., Takagishi, M., Shiromizu, T., Saitoh, N., Izawa, I., Kiyono, T., Itoh, T. J., Hotani, H. et al. (2003). Filament formation of MSF-A, a mammalian septin, in human mammary epithelial cells depends on interactions with microtubules. *J. Biol. Chem.* **278**, 18538-18543.
Nandadasa, S., Tao, Q., Menon, N. R., Heasman, J. and Wylie, C. (2009). N- and E-cadherins in Xenopus are specifically required in the neural and non-neural ectoderm, respectively, for F-actin assembly and morphogenetic movements. *Development* **136**, 1327-1338.
Nishimura, T., Honda, H. and Takeichi, M. (2012). Planar cell polarity links axes of spatial dynamics in neural-tube closure. *Cell* **149**, 1084-1097.
Nölke, T., Schwan, C., Lehmann, F., Østevold, K., Pertz, O. and Aktories, K. (2016). Septins guide microtubule protrusions induced by actin-depolymerizing toxins like Clostridium difficile transferase (CDT). *Proc. Natl. Acad. Sci. USA* **113**, 7870-7875.
Sellin, M. E., Stenmark, S., Gullberg, M. and Kellogg, D. (2012). Mammalian SEPT9 isoforms direct microtubule- dependent arrangements of septin core heteromers. *Mol. Biol. Cell* **23**, 4242-4255.
Shindo, A. and Wallingford, J. B. (2014). PCP and septins compartmentalize cortical actomyosin to direct collective cell movement. *Science* **343**, 649-652.
Shindo, A., Yamamoto, T. S. and Ueno, N. (2008). Coordination of cell polarity during Xenopus gastrulation. *PLoS ONE* **3**, e1600.
Sirajuddin, M., Farkasovsky, M., Hauer, F., Kühlmann, D., Macara, I. G., Weyand, M., Stark, H. and Wittinghofer, A. (2007). Structural insight into filament formation by mammalian septins. *Nature* **449**, 311-317.
Soto, X., Li, J., Lea, R., Dubaissi, E., Papalopulu, N. and Amaya, E. (2013). Inositol kinase and its product accelerate wound healing by modulating calcium levels, Rho GTPases, and F-actin assembly. *Proc. Natl. Acad. Sci. USA* **110**, 11029-11034.
Spiliotis, E. T. (2010). Regulation of microtubule organization and functions by septin GTPases. *Cytoskeleton (Hoboken)* **67**, 339-345.
Stanisstreet, B. M., Wakely, J. and England, M. A. (1980). Scanning electron microscopy of wound healing in Xenopus and chicken embryos. *J. Embryol. Exp. Morphol.* **59**, 341-353.
Surka, M. C., Tsang, C. W. and Trimble, W. S. (2002). The mammalian septin MSF localizes with microtubules and is required for completion of cytokinesis. *Mol. Biol. Cell* **13**, 3532-3545.
Suzuki, M., Sato, M., Koyama, H., Hara, Y., Hayashi, K., Yasue, N., Imamura, H., Fujimori, T., Nagai, T., Campbell, R. E. et al. (2017). Distinct intracellular Ca^{2+} dynamics regulate apical constriction and differentially contribute to neural tube closure. *Development*, 144, 1307-1316.
Wasik, A. A., Dumont, V., Tienari, J., Nyman, T. A., Fogarty, C. L., Forsblom, C., Lehto, M., Lehtonen, E., Groop, P.-H. and Lehtonen, S. (2017). Septin 7 reduces nonmuscle myosin IIA activity in the SNAP23 complex and hinders GLUT4 storage vesicle docking and fusion. *Exp. Cell Res.* **350**, 336-348.
Weirich, C. S., Erzberger, J. P. and Barral, Y. (2008). The septin family of GTPases : architecture and dynamics. *Nat. Rev. Mol. Cell Biol.* **9**, 478-489.
Wühr, M., Tan, E. S., Parker, S. K., Detrich, H. W. and Mitchison, T. J. (2010). A model for cleavage plane determination in early amphibian and fish embryos. *Curr. Biol.* **20**, 2040-2045.
Xie, Y., Vessey, J. P., Konecna, A., Dahm, R., Macchi, P. and Kiebler, M. A. (2007). The GTP-binding protein septin 7 Is critical for dendrite branching and dendritic-spine morphology. *Curr. Biol.* **17**, 1746-1751.
Yu, J. C. and Fernandez-Gonzalez, R. (2016). Local mechanical forces promote polarized junctional assembly and axis elongation in Drosophila. *Elife* **5**, e10757.
Zallen, J. A. and Wieschaus, E. (2004). Patterned gene expression directs bipolar planar polarity in Drosophila. *Dev. Cell* **6**, 343-355.
Zulueta-Coarasa, T., Tamada, M., Lee, E. J. and Fernandez-Gonzalez, R. (2014). Automated multidimensional image analysis reveals a role for Abl in embryonic wound repair. *Development* **141**, 2901-2911.